Controlled Growth of Porous α-Fe_2O_3 Branches on β-MnO_2 Nanorods for Excellent Performance in Lithium-Ion Batteries

Xin Gu, Liang Chen, Zhicheng Ju, Huayun Xu, Jian Yang, and Yitai Qian*

Hierarchical nanocomposites rationally designed in component and structure, are highly desirable for the development of lithium-ion batteries, because they can take full advantages of different components and various structures to achieve superior electrochemical properties. Here, the branched nanocomposite with β-MnO_2 nanorods as the back-bone and porous α-Fe_2O_3 nanorods as the branches are synthesized by a high-temperature annealing of FeOOH epitaxially grown on the β-MnO_2 nanorods. Since the β-MnO_2 nanorods grow along the four-fold axis, the as-produced branches of FeOOH and α-Fe_2O_3 are aligned on their side in a nearly four-fold symmetry. This synthetic process for the branched nanorods built by β-MnO_2/α-Fe_2O_3 is characterized. The branched nanorods of β-MnO_2/α-Fe_2O_3 present an excellent lithium-storage performance. They exhibit a reversible specific capacity of 1028 mAh g^{-1} at a current density of 1000 mA g^{-1} up to 200 cycles, much higher than the building blocks alone. Even at 4000 mA g^{-1}, the reversible capacity of the branched nanorods could be kept at 881 mAh g^{-1}. The outstanding performances of the branched nanorods are attributed to the synergistic effect of different components and the hierarchical structure of the composite. The disclosure of the correlation between the electrochemical properties and the structure/component of the nanocomposites, would greatly benefit the rational design of the high-performance nanocomposites for lithium ion batteries, in the future.

1. Introduction

Rechargeable lithium-ion batteries (LIBs) have attracted extensive attention in the past decade, because they have been regarded as one of important energy-storage technologies to support the sustainable usage of green and clean energy sources like solar, wind, tide, and so forth. Since the practical applications of LIBs highly rely on the performance of electrodes, how to design and achieve high-efficient, low-cost and safe electrode materials turns into a great challenge to both academia and industries. Compared with the conventional carbon-based material, transition metal oxides as negative electrodes offer more choices to realize the high reversible capacities by different pathways, such as alloying/dealloying processes (SnO_2), insertion/extraction mechanisms (TiO_2, $Li_4Ti_5O_{12}$) and conversion reactions (Fe_2O_3, Co_3O_4, MnO_2).[1] Assembly of different oxides into a hierarchical nanocomposite would allow us to make use of their interaction for the better performances in LIBs. Based on this concept, a few nanocomposites built by different oxides have been examined for LIBs, such as Fe_2O_3/SnO_2, Fe_2O_3/TiO_2, Fe_2O_3/ZnO, TiO_2/SnO_2, and so on.[2]

Fan and co-workers reported the synthesis of SnO_2 nanowire-supported α-Fe_2O_3 nanorods by a chemical vapor deposition, followed with a hydrothermal reaction.[2d] Although this heterogeneous nanostructure exhibited a good control on the growth of building blocks, it did not show an excellent lithium-storage performance, as expected. After 30 cycles, the heterogeneous nanostructure only presented ≈250 mAh g^{-1} at a current density of 1000 mA g^{-1}, which is almost the same as those from the single components. Recently, the same group developed a stepwise hydrothermal process to prepare core-shell TiO_2@Fe_2O_3 nanorods on a carbon cloth. The obtained composite displayed a reversible capacity of 480 mAh g^{-1} at 120 mA g^{-1} after 150 cycles, much higher than those of carbon cloth and TiO_2 nanorods on the carbon cloth. Unfortunately, the comparison between the composite and Fe_2O_3 was missed, which is important to confirm the synergistic effect of all the components.[2g] Lou and co-workers fabricated Fe_2O_3@SnO_2 nanorattles through an inside-out Ostwald ripening process occurred to SnO_2. Although the nanorattles reduced the irreversible capacity loss of the first cycle, they only exhibited a capacity of 419 mAh g^{-1} at a rate of 200 mAg^{-1} after 30 cycles.[2a] Mullins and team reported a co-precipitation

X. Gu, L. Chen, Dr. H.Y. Xu, Prof. J. Yang,
Prof. Y.T. Qian
Key Laboratory of Colloid and Interface Chemistry
Ministry of Education
School of Chemistry and Chemical Engineering
Shandong University
Jinan, 250100, P. R. China
E-mail: yangjian@sdu.edu.cn
Dr. Z. C. Ju, Prof. Y.T. Qian
Hefei National Laboratory for Physical Science at Microscale
Department of Chemistry
University of Science and Technology of China
Hefei, 230026, P. R. China

DOI: 10.1002/adfm.201203779

method for SnO_2/TiO_2 nanocomposite in a size of 10 nm. Such a composite delivered a specific capacity of ≈320 mAh g^{-1} at a rate of 0.2 C after 100 cycles.[3] The performances of all these nanocomposites are far away from being satisfactory. One of the possible reasons is due to the absence of the proper selection of the chemical component.

Herein, MnO_2 and Fe_2O_3 are selected to construct the composite, due to their high theoretical capacities (1232 mAh g^{-1} for MnO_2, and 1007 mAh g^{-1} for Fe_2O_3), high abundance and low toxicity. Although both of them suffer from severe volume change and poor electronic conductivity, the cycling stability and rate capability of MnO_2 nanostructures are much worse than those of Fe_2O_3.[4] Thus, Fe_2O_3 is designed to coat the surface of MnO_2, to bridge it with the electrolyte. Meanwhile, the surface coating of Fe_2O_3 on MnO_2 might restrain the potential dissolution of Mn species into electrolyte during lithiation/delithiation. The further control of MnO_2 as the backbone and Fe_2O_3 as the branches would leave plenty of room to tolerate the volume change during the discharge/charge process, improving the cycling stability of electrodes.[2b,2e,5] To the best of our knowledge, such a composite built by MnO_2 and Fe_2O_3 has not been synthesized and explored before. To synthesize these α-Fe_2O_3 branch-coated β-MnO_2 nanorods, FeOOH is firstly grown on the tetragonal-phase β-MnO_2 nanorods by a hydrothermal reaction, generating a large number of the branches in a nearly four-fold symmetry. Then, these branched β-MnO_2/FeOOH nanorods are annealed at a high temperature, resulting in the β-MnO_2 nanorods coated with porous α-Fe_2O_3 branches. The whole process for the branched nanorods is characterized by X-ray diffraction (XRD) patterns, scanning electron microscopy (SEM) images, transmission electron microscopy (TEM) images, high-resultion TEM (HRTEM) images and selected area electron diffraction (SAED) patterns. The branched nanorods of β-MnO_2/α-Fe_2O_3 exhibit excellent lithium-storage performances in terms of reversible capacity, cycling stability and rate capability, which could be assigned to the synergistic effect of different components and the hierarchical structure of the nanocomposite. These results indicate the importance of the elaborate selection of the chemical components and the rational design of the hierarchical structure, based on the fundamental principles of LIBs.

2. Results and Discussion

Figure 1 presents the XRD patterns of the products obtained at different stages of the synthesis process. The product prepared by the pyrolysis of MnOOH nanorods, could be identified as tetraganol-phase β-MnO_2 (JCPDS Card, No 24-0735), as shown in Figure 1a. The calculated lattice constants are 4.38 Å for *a* and 2.88 Å for *c*, very close to the reported values (*a* = 4.40 Å and *c* = 2.87 Å). However, the intensity ratios of (110) and the other reflections differ a lot from the standard. This result could be explained by the preferential growth of crystals, which has been documented in a variety of one-dimensional nanomaterials.[6] The low-temperature hydrolysis of $FeCl_3$ in the presence of β-MnO_2 produces orthorhombic-phase FeOOH (JCPDS Card, No 29-0713), as illustrated in Figure 1b. The broad and weak diffraction peaks of FeOOH indicate its poor crystallinity, which

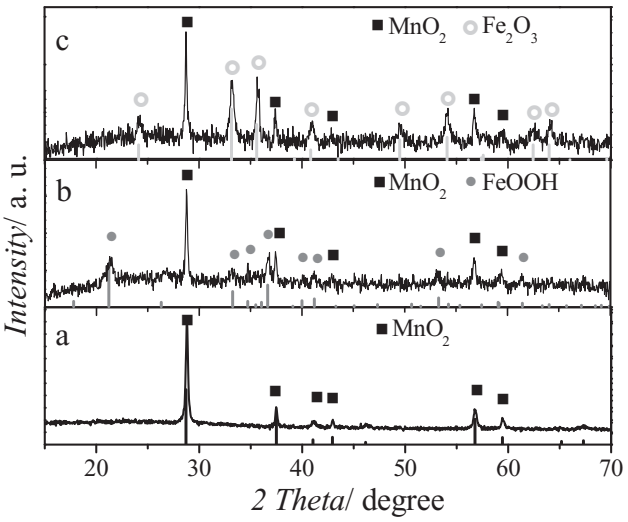

Figure 1. XRD patterns of a) β-MnO_2 nanorods, b) branched nanorods of β-MnO_2/FeOOH, c) branched nanorods of β-MnO_2/α-Fe_2O_3.

could be attributed to the low reaction temperature. High-temperature annealing of this product results in the formation of rhombohedral-phase α-Fe_2O_3 (JCPDS Card, No 33–0664), as described in Figure 1c. It should be noted that tetraganol-phase β-MnO_2 is preserved throughout the entire process, although its crystallinitiy is significantly reduced in comparison to that before the reaction.

Figure 2 shows the field emission SEM (FESEM) images of the products obtained at different stages of the synthesis process. The FESEM images of the as-obtained β-MnO_2 are presented in Figure 2a and 2b, where the nanorods with a smooth surface dominate the product. These β-MnO_2 nanorods are 30–120 nm in diameter and 2–10 μm in length. After a hydrothermal reaction for FeOOH, a large number of tiny nanorods are deposited on the surface of the β-MnO_2 nanorods (Figure 2c,d). These tiny nanorods with their average diameter of 30 nm and length of 140 nm, are basically perpendicular to the side facets of the β-MnO_2 nanorods, producing a typical branched nanostructure. Furthermore, the distribution of the tiny nanorods around the β-MnO_2 nanorods presents a nearly four-fold symmetry, which is emphasized by a white line in the inset of Figure 2d. The result could be correlated with the growth of the β-MnO_2 nanorods along the four-fold axis, which makes the four side facets identical for the deposition of FeOOH. The yield of the branched nanostructures is so high that the β-MnO_2 nanorods with a smooth surface are not observed in the product. Figure S1 in the Supporting Information describes the evolution process from the β-MnO_2 nanorods to the branched nanorods of β-MnO_2/FeOOH. High-temperature annealing of these branched nanorods for β-MnO_2/α-Fe_2O_3 does not change the branched morphology (Figure 2e,f). The formation of such a branched nanostructure implies the increased reactive sites and interface areas during the discharge/charge processes, both of which would facilitate this material to achieve a high specific capacity.[2b,2d,2e] It should be pointed out that the branched nanorods based on β-MnO_2 with a nearly four-fold symmetry are synthesized for the first time. The synthetic process for the

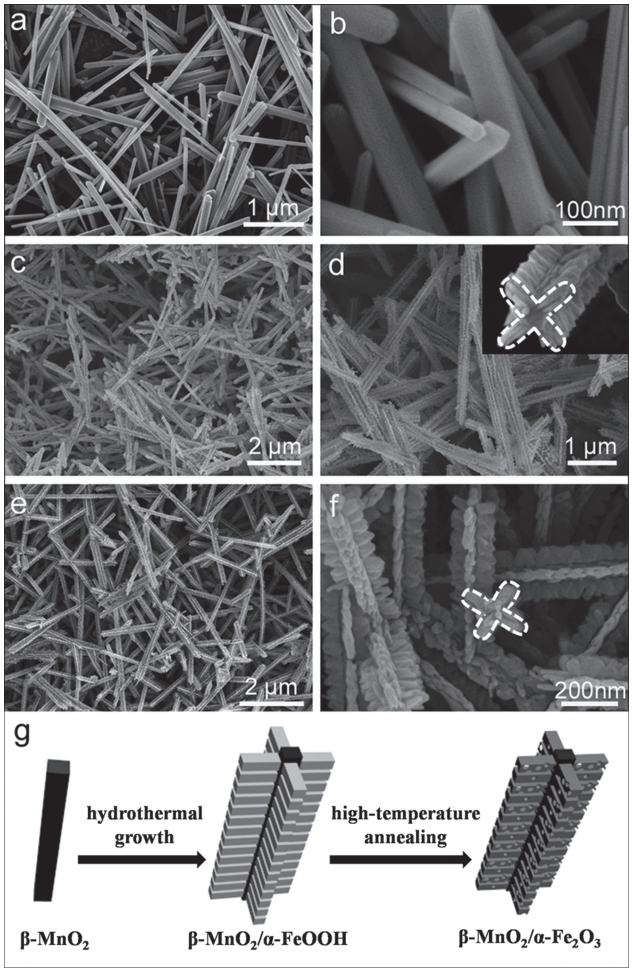

Figure 2. FESEM images of a,b) β-MnO_2 nanorods; c,d) branched nanorods of β-MnO_2/FeOOH; e,f) branched nanorods of β-MnO_2/α-Fe_2O_3; g) Schematic illustration of the synthetic process of the branched nanostructures of β-MnO_2/α-Fe_2O_3.

branched nanorods of β-MnO_2/α-Fe_2O_3 could be summarized in the Figure 2g. First, the β-MnO_2 nanorods are prepared by the pyrolysis of MnOOH nanorods under mild experiment conditions. Then, the as-obtained β-MnO_2 nanorods are employed as a seed to induce the epitaxial growth of FeOOH on their surface, producing the branched nanorods. Finally, the branched nanorods of β-MnO_2/FeOOH are annealed at a relatively low temperature to produce the α-Fe_2O_3 branches on the β-MnO_2 nanorods. Since the pyrolysis of FeOOH is a dehydration reaction, it is likely to form a large number of tiny pores in the α-Fe_2O_3 branches, which has been directly confirmed by TEM images and BET measurements.

Figure 3 shows the TEM images, HRTEM images and SAED patterns of the products obtained at different stages of the synthesis process. A typical TEM image of a single β-MnO_2 nanorod is presented in Figure 3a. Correlated with the SAED pattern on this nanorod, it can be concluded that the single-crystal nanorod grows along the direction of *c* axis. This result well explains the difference of the XRD pattern in our case from the standard one. Figure 3b shows a TEM image of a single branched nanorod of β-MnO_2/FeOOH. Since TEM images are the planar projection of three-dimensional structures and the nanorods are inclined to lay down on the surface of the copper grids, the four-fold symmetry of FeOOH around the β-MnO_2 nanorods is not observed in the TEM image. The enclosed area at the interface of β-MnO_2 and FeOOH is magnified to understand the crystallographic connection between them, as highlighted by the white square of the TEM image. As illustrated in Figure 3c, the interface between FeOOH and β-MnO_2 shows a typical single-crystal feature, indicating the epitaxial growth of FeOOH on β-MnO_2. The further examination on the HRTEM image clearly confirms the lattice fringes of $(021)_{FeOOH}$, $(02\text{-}1)_{FeOOH}$, $(001)_{FeOOH}$, $(101)_{MnO2}$, $(10\text{-}1)_{MnO2}$, and $(001)_{MnO2}$ beside the interface. Based on the results, the interface between MnO_2 and FeOOH can be identified as $(010)_{FeOOH}//(100)_{MnO2}$. This epitaxial growth is also supported by their crystal structures, as shown in Figure 3d. The lattice mismatches between $(100)_{MnO2}$ and $(010)_{FeOOH}$ are 4.87% along $c_{MnO2}//c_{FeOOH}$ (c_{MnO2} = 2.874 Å, c_{FeOOH} = 3.021 Å) and 4.51% along $b_{MnO2}//a_{FeOOH}$ (b_{MnO2} = 4.399 Å, a_{FeOOH} = 4.608 Å), both of which are small enough to be tolerated for the epitaxial growth. The similar conclusion has been also verified by the fast Fourier transformation (FFT) patterns, as shown in the insets of Figure 3c. Figure 3e presents a typical TEM image of a single branched nanorod of β-MnO_2/α-Fe_2O_3 obtained by the annealing of the branched nanorods of β-MnO_2/FeOOH. As expected, the α-Fe_2O_3 branches display a porous structure, due to the decomposition of FeOOH. A similar structure is also observed in the pyrolysis of FeOOH nanorods for α-Fe_2O_3 nanorods (Supporting Information, Figure S2). As suggested by Figure 3f, the as-obtained α-Fe_2O_3 branches are polycrystalline. Thus, there is no specific relationship between α-Fe_2O_3 branches and β-MnO_2 nanorods in crystallographics. The molar ratio of Mn:Fe in the branched nanorods is approximately 1:2.73, as revealed by the EDS spectrum (Supporting Information, Figure S3).

The porous structure in the branched nanorods of β-MnO_2/α-Fe_2O_3 is characterized by Brunauer-Emmett-Teller (BET) measurements, as shown in **Figure 4**. The nitrogen sorption isotherm gives an obvious hysteresis loop, indicating the mesoporous structures in the composite. The specific surface area and pore volume of the branched nanorods are 32.7 m^2 g^{-1} and 0.119 cm^3 g^{-1}, respectively. As calculated by the Barrett-Joyner-Halenda (BJH) method, the average pore size is approximately 7.6 nm, which is in accordance with that from TEM images.

The electrochemical properties of the branched nanorods of β-MnO_2/α-Fe_2O_3 as an anode material for LIBs, are examined by cyclic voltammograms, using a Li foil as the counter and reference electrode. As shown in **Figure 5**a, the two cathodic peaks at 1.02 and 0.21 V in the first cycle, could be assigned to the reductions of MnO_2 to Mn^{2+} and Mn^{2+} to Mn^0.[4d,7] The three peaks at 1.63, 0.99 and 0.70 V correspond to the formation of α-$Li_xFe_2O_3$, the phase transition from α-$Li_xFe_2O_3$ to c-$Li_2Fe_2O_3$, the complete reduction of c-$Li_2Fe_2O_3$ to Fe^0 and the formation of SEI film respectively.[8] These results indicate that the appearance of Fe^0 in the electrode is ahead of the reduction of Mn^{2+} to Mn^0. Since the α-Fe_2O_3 branches locate at the exterior of the branched nanorods, the as-produced metallic Fe would directly contact with the electrolyte and then increase the electron

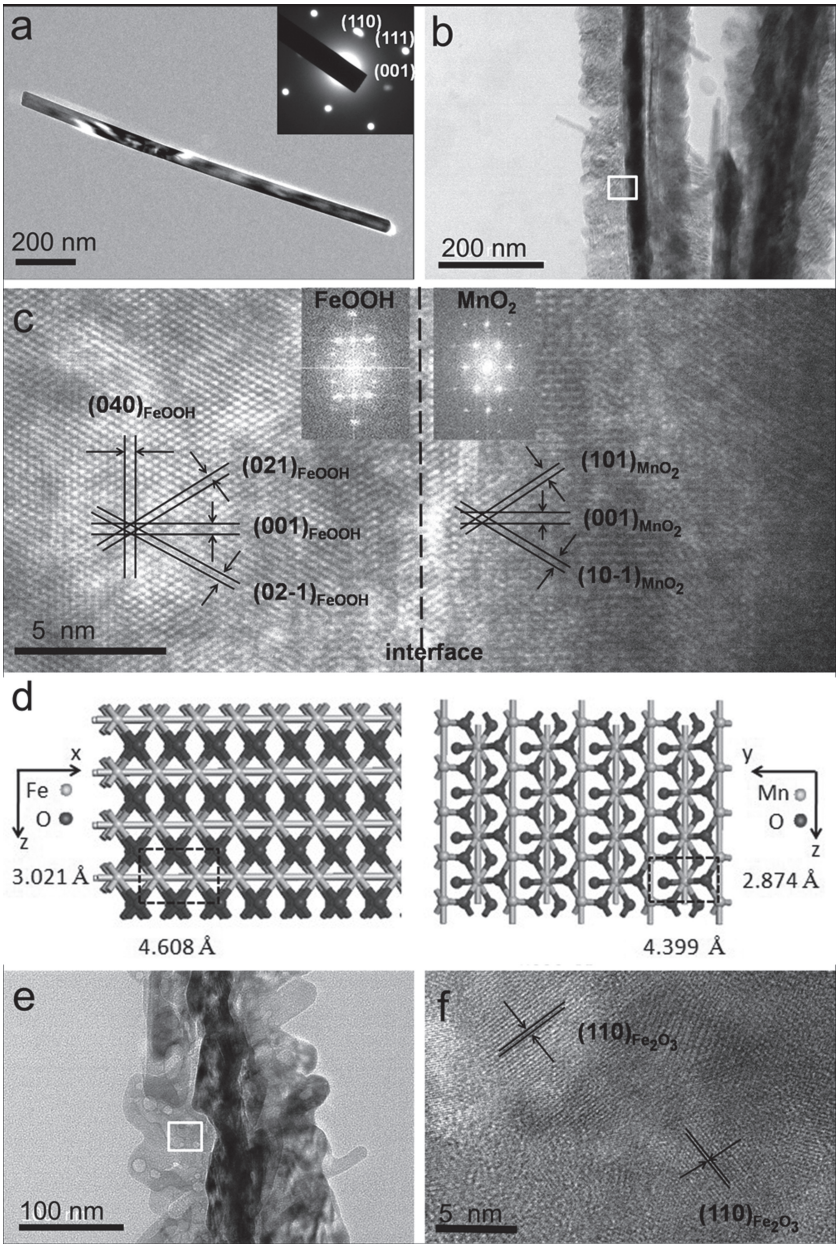

Figure 3. a) TEM image and SEAD pattern of a single β-MnO_2 nanorod. b) TEM image of the branched nanorods of β-MnO_2/FeOOH. The area in the white square of this TEM image is magnified for c) HRTEM image. The inset of the HRTEM images are the fast Fourier transformation (FFT) patterns of β-MnO_2 and FeOOH beside the interface. d) Crystal structures of $(010)_{FeOOH}$ (left) and $(100)_{MnO2}$ (right). e) TEM image of a branched nanorod of β-MnO_2/α-Fe_2O_3. The area in the white square of the TEM image is magnified for f) HRTEM image.

conductivity of the entire composite, facilitating the later formation of Mn^0. After the first cycle, the two intense peaks slightly shift to 0.82 and 0.31 V, due to the structure reconstruction induced by the formation of Li_2O and metals.[4c,7,9] The results are in good agreement with those from the β-MnO_2 nanorods and the porous α-Fe_2O_3 nanorods (Supporting Information, Figure S4). The anodic scanning gives four peaks at 1.28, 1.61, 1.87 and 2.07 V. The two peaks at 1.61 and 1.87 V come from the oxidation of Fe^0 into Fe^{3+}, which is very close to those observed in the case of the porous α-Fe_2O_3 nanorods. Compared with the data from the β-MnO_2 nanorods, one of the peaks moves from 1.23 to 1.28 V for the branched nanorods and the other shifts from 2.27 to 2.07 V. The former could be assigned to the shielding effect of Fe at the exterior of the branched nanorods on the electrochemical oxidation of Mn^0 to Mn^{2+}. The latter might be attributed to the effect of Fe_2O_3 on the electrochemical oxidation of Mn^{2+} into Mn^{4+}, because Fe_2O_3 is formed before this oxidation reaction and then contains Mn species in the center. This result indicates that metallic Mn could be oxidized into MnO_2 under a lower potential, suggesting a less electrode polarization and a lower energy-loss for discharge-charge. Meanwhile, the presence of Fe_2O_3 at the exterior of the composite also effectively separates the as-obtained β-MnO_2 from the electrolyte, avoiding the possible dissolution of Mn species and other side-effects.

Figure 5b shows the first discharge-charge profiles for Li/β-MnO_2 nanorods, Li/α-Fe_2O_3 nanorods, and Li/branched β-MnO_2/α-Fe_2O_3 nanorods at a current density of 100 mA g^{-1} in the range of 0.01–3.0 V. The discharge/charge profiles of the branched β-MnO_2/α-Fe_2O_3 nanorods can be regarded as a combination of those of β-MnO_2 and α-Fe_2O_3 nanorods, which is also consistent with that obtained from CV measurements. The initial discharge capacities of the β-MnO_2 nanorods, the α-Fe_2O_3 nanorods and the branched β-MnO_2/α-Fe_2O_3 nanorods are 1734, 1646 and 1480 mAh g^{-1}. All of them are higher than their theoretical capacities, which could be attributed to the decomposition of the electrolyte to form a SEI layer on the surface of electrode.[10] Meanwhile, the branched nanorods show a higher initial coulombic efficiency about 77.5%, compared with the β-MnO_2 nanorods at 72% and the α-Fe_2O_3 nanorods at 71.7%. The improved coulombic efficiency for the branched nanorods, might be attributed to the increased reversibility of the involved electrochemical reactions, which is also supported by CV measurements. A similar phenomenon was reported by Fan and co-workers in branched α-Fe_2O_3/SnO_2 nanostructures.[2d] They claimed that the increased coulombic efficiency of the composite came from the improved reversibility of the oxidation from Sn^0 to SnO_2. Unfortunately, no direct evidences from CV profiles or TEM images were presented to support this point.

Figure 5c shows the cycling performance of Li/β-MnO_2 nanorods, Li/α-Fe_2O_3 nanorods, and Li/branched nanorods of β-MnO_2/α-Fe_2O_3 in the range of 0.01–3.0 V. The first five cycles are conducted at a current density of 100 mA g^{-1}

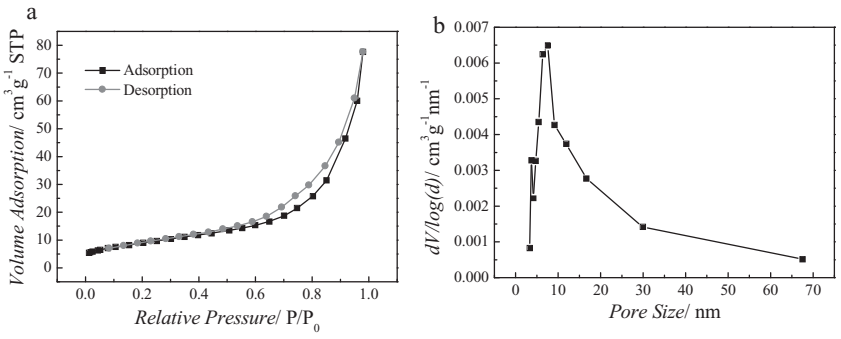

Figure 4. a) Nitrogen adsorption-desorption isotherms and b) pore-size-distribution curves of the branched nanorods of β-MnO_2/α-Fe_2O_3.

to activate the electrode materials. Then, the current density is increased to 1000 mA g^{-1} for the later cycling. As a result, the branched β-MnO_2/α-Fe_2O_3 nanorods deliver a reversible capacity of 1028 mAh g^{-1} after 200 cycles, very close to the theorectical capacity of the branched β-MnO_2/α-Fe_2O_3 nanorods (1071 mAh g^{-1} = 1232 mAh g^{-1} × 28.6 wt% (β-MnO_2) + 1007 mAh g^{-1} × 71.4 wt% (α-Fe_2O_3)). This data is also much higher than those of β-MnO_2 nanorods (283 mAh g^{-1}), porous α-Fe_2O_3 nanorods (314 mAh g^{-1}), and the MnO_2-based or Fe_2O_3-based composites, as summarized in **Table 1**. For instance, the MnO_2-coated carbon nanotube (CNT) arrays only exhibited a reversible capacity of ≈500 mAh g^{-1} at a current density of 50 mA g^{-1} after 15 cycles.[4e] Using carbon nanohorns to replace CNTs could improve the specific capacity to 565 mAh g^{-1} at a rate of 450 mA g^{-1} after 60 cycles.[11] After hybridized with graphene and conductive polymers together, the MnO_2-based composite displayed a specific capacity up to 948 mAh g^{-1}.[12] But the current density and the cycle number had to be reduced to 50 mA g^{-1} and 15 cycles. The superior cycling performance is also demonstrated in comparison to the Fe_2O_3-based nanocomposites. Branched α-Fe_2O_3/SnO_2 nanostructures delivered a specific capacity of ≈250 mAh g^{-1} at a current density of 1000 mA g^{-1} after 30 cycles.[2d] Using SnO_2 nanosheets to replace the SnO_2 nanowires for the Fe_2O_3-SnO_2 nanocomposite would generate a reversible capacity of 325 mAh g^{-1} at 400 mA g^{-1} after 50 cycles.[2b] For core-shell TiO_2@Fe_2O_3 nanorods grown on the carbon textiles, only a reversible capacity of 480 mAh g^{-1} was maintained at 120 mA g^{-1} after 150 cycles.[2g] The even more complicate heterogeneous nanostructures like TiO_2 nanotubes-supported hollow α-Fe_2O_3 only showed a specific capacity of ≈380 mAh g^{-1}.[2h]

The outstanding performance of the branched nanorods in LIBs is also confirmed at different rates. As shown in Figure 5d, the branched β-MnO_2/α-Fe_2O_3 nanorods exhibit the reversible capacities of 1173, 1060, 971 and 881 mAh g^{-1} at the current densities of 100, 500, 1000, 2000 and 4000 mA g^{-1}, respectively. As the rate is back to 100 mA g^{-1}, the specific capacity of the branched nanorods returns to 1350 mAh g^{-1}, suggesting the

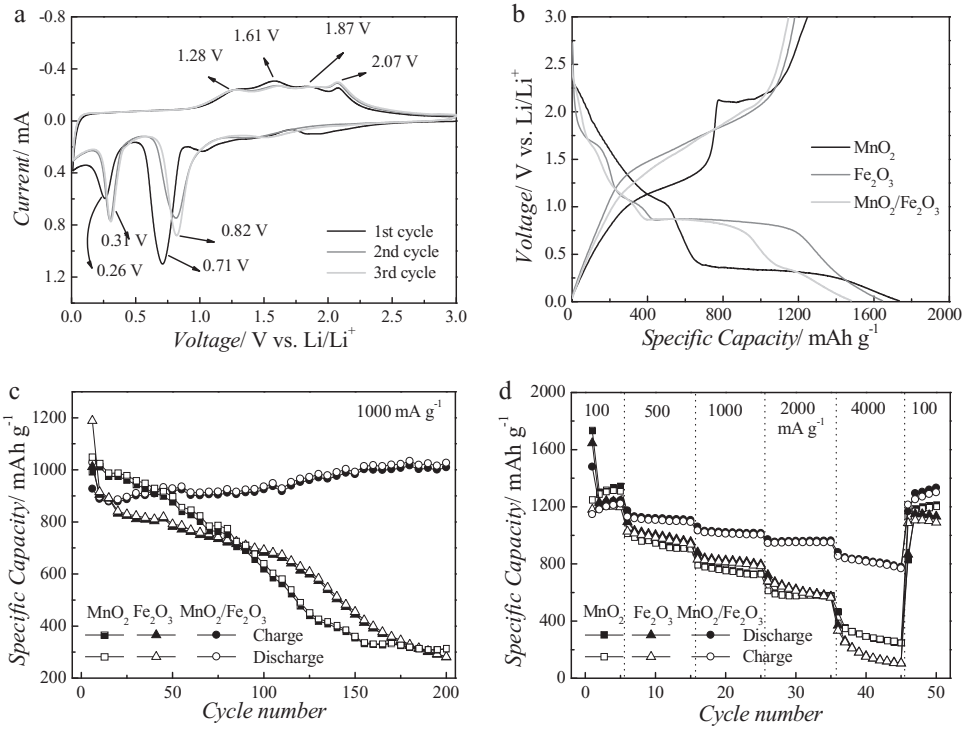

Figure 5. a) Cyclic voltammograms (CVs) of the branched nanorods of β-MnO_2/α-Fe_2O_3 at a scanning rate of 0.1 mV s^{-1}. b) First discharge-charge curves, c) cycling performance and d) rate performance of the electrodes based on the β-MnO_2 nanorods, the porous Fe_2O_3 nanorods and the branched nanorods of β-MnO_2/α-Fe_2O_3.

Table 1. The cycling performances of some reported hybrid nanostructures.

Hybrid Nanomaterials	Current density [mA g^{-1}]	Cycle Number	Capacity [mAh g^{-1}]	Ref.
Coaxial MnO_2/CNT Array	50	15	≈500	[4e]
MnO_2/Conjugated Polymer/ Graphene	50	15	948	[12]
TiO_2 nanotubes-supported hollow α-Fe_2O_3	100[a)]	50	≈380	[2h]
TiO_2@α-Fe_2O_3 core/shell arrays on carbon textiles	120	150	480	[2g]
Fe_2O_3/SnO_2 nanocombs	400	50	325	[2b]
Flower-like ZnO/Fe_2O_3 nanostructures	400	50	776	[2i]
MnO_2/Carbon Nanohorns	450	60	565	[11]
Branched α-Fe_2O_3/SnO_2	1000	30	≈250	[2d]
Branched Fe_2O_3 on MnO_2 nanorods	1000	200	1028	Our work

[a)]The unit of this current density is μA cm^{-2}.

good rate capacity and structure stability of the active material. The extra capacity might arise from the insertion of lithium into acetylene black,[13] and interfacial storage.[14] The rate performance of the branched nanorods is not only much better than those of the β-MnO_2 nanorods and the porous α-Fe_2O_3 nanorods, but also much higher than most of the related works. For example, core-shell TiO_2@α-Fe_2O_3 branches grown on carbon textiles only present a reversible capacity of 121 mAh g^{-1} at 960 mA g^{-1}.[2g] Flower-like ZnO/Fe_2O_3 nanostructures exhibited a specific capacity of 580 mAh g^{-1} at 2000 mA g^{-1}.[2i] The high reversible capacity, excellent cycling performance and superior rate capability in our case could be attributed to hierarchical structure built by branches and tiny pores, and synergistic effect of the two components. The former would greatly increase the specific surface areas of the active material and reduce the intrinsic strain/stress caused by the severe volume change.[2b,2d,2e] This conclusion could be verified by BET measurements. The branched nanorods give a specific surface area of 32.7 m^2 g^{-1}, larger than β-MnO_2 nanorods about 9.7 m^2 g^{-1} and porous α-Fe_2O_3 nanorods about 23.3 m^2 g^{-1}. The synergistic effect of the two components in our case effectively improves the reversibility of the electrochemical reaction, buffers the huge strain/stress during the discharge-charge processes, and prevents the aggregation of active materials.[2f,2m,15] For example, during the discharge process, the preferential formation of Fe^0 increases the electron conductivity of the composite and then facilitates the subsequent reduction of Mn^{2+} to Mn^0. Meanwhile, MnO_x acts as a matrix to restrain the aggregation of newly-formed Fe^0 and accommodate the volume change induced by the reduction of Fe_2O_3. In the charge process, the preferential oxidation of Fe^0 to Fe_2O_3 lowers the oxidation voltage of Mn^{2+} to Mn^{4+},

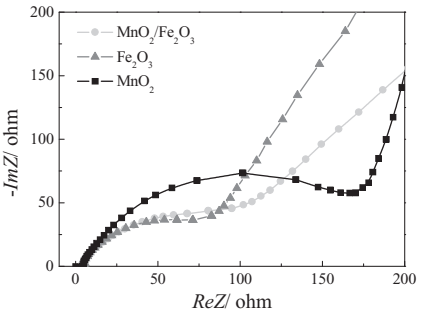

Figure 6. Nyquist plots of the AC impedance spectra for the electrodes based on the β-MnO_2 nanorods, the porous Fe_2O_3 nanorods and branched nanorods of β-MnO_2/α-Fe_2O_3.

and reduces the electrode polarization. All of them make positive contributions to the fast and reversible insertion/extraction of lithium. Thus, the specific capacity of the branched nanorods could be well preserved after a long-term cycling even under a high rate.[2c,2k]

Electrochemical impedance spectra (EIS), both AC and DC impedance spectra (current interrupt), are measured to get more insights for the superior performance of the branched nanorods.[16] As shown in **Figure 6**, all the AC impedance spectra of the electrodes based on α-Fe_2O_3, β-MnO_2 and the branched nanorods of β-MnO_2/α-Fe_2O_3 exhibit the typical Nyquist plots composed by a semicircle at the high-to-medium frequency region and a slope line at the low frequency region. This semicircle is attributed to the charge transfer resistance (R_{ct}) between the electrolyte and the electrode. The slope line might be related with the Warburg impedance (Z_w) induced by lithium diffusion in the electrodes. Based on this fitting model, the R_{ct}s of the electrodes based on α-Fe_2O_3, β-MnO_2 and the branched nanorods are 70, 174 and 80 Ω, respectively. The results indicate that the presence of α-Fe_2O_3 in the branched nanorods greatly promote the charge transfer at the electrode/electrolyte interface, and thus benefit the electrochemical performance. The similar conclusion is also concluded from DC impedance spectra. As shown in **Figure 7**, the branched nanorods of β-MnO_2/α-Fe_2O_3 show a DC resistance (R_{dc}) smaller than that of the β-MnO_2 nanorods, particularly at the beginning of the discharge process or at the end of the charge process. This result indicates that the presence of the α-Fe_2O_3

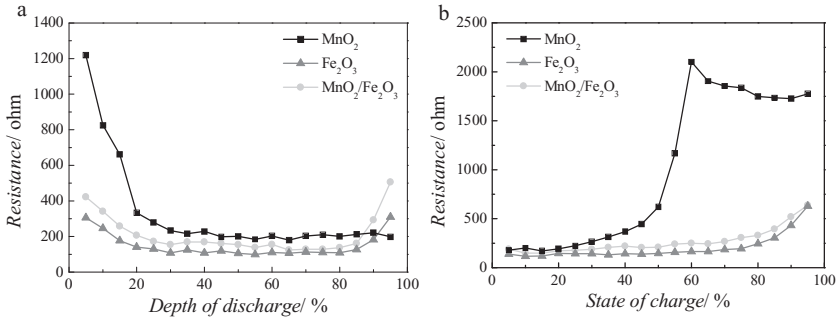

Figure 7. The direct current resistance (R_{dc}) of the β-MnO_2 nanorods, the porous Fe_2O_3 nanorods and the branched nanorods of β-MnO_2/α-Fe_2O_3 versus a) depth of discharge or b) state of charge.

branches could effectively reduce the DC resistance of the branched nanorods, facilitating the electron transportation.

3. Conclusions

In summary, branched nanorods composed by β-MnO_2 nanorods as a backbone and porous α-Fe_2O_3 nanorods as the branches, are successfully synthesized by the decomposition of FeOOH epitaxially grown on the β-MnO_2 nanorods. In this hierarchical structure, the well-aligned α-Fe_2O_3 branches are nearly perpendicular to the side facets of the β-MnO_2 nanorods, generating a nearly four-fold symmetry along the axial direction of the nanorods. This structure feature could be attributed to the unique crystallographic connection between FeOOH and β-MnO_2, $(010)_{FeOOH}//(100)_{MnO2}$, which has been identified by HRTEM images and FFT patterns. TEM images further reveal the porous feature of the α-Fe_2O_3 branches, which originates from the decomposition of FeOOH. Electrochemical measurements suggest that the branched nanorods exhibit an excellent performance in terms of reversible specific capacity, cycling stability and rate performance. The branched nanorods delivered a specific capacity of 1027.7 mAh g^{-1} at a current density of 1000 mA g^{-1} after 200 cycles, much higher than those from the single components and the reported nanocomposites. At a rate of 4000 mA g^{-1}, the reversible capacity of the branched nanorods could be as high as 881 mAh g^{-1}. This excellent performance of the branched nanorods is assigned to the hierarchical structure built by branches and tiny pores, and synergistic effect of different components. These results indicate the importance of the selection of proper chemical components and the control on their construction. The combination of the advantages in structure and components would effectively improve the performance of electrode materials in LIBs. Besides, the hierarchical structures constructed by multi-components would also present great application rooms in the fields of supercapacitors, chemical sensors and solar energy conversion.

4. Experimental Section

Sample Synthesis: The synthesis of the branched nanorods of β-MnO_2/α-Fe_2O_3 was started from the β-MnO_2 nanorods prepared by annealing MnOOH nanorods at 280 °C for 2 h.[17] The as-prepared β-MnO_2 nanorods (20 mg) were dispersed into deionized water (10 mL) by ultrasonication. Then, $FeCl_3$ (≥ 99.5%, 1.5 mmol), $NaNO_3$ (≥ 99.5%, 10 mmol) and hydrochloric acid (36–38%, 20 μL) were added into the above solution. After stirred for 30 min, the solution was transferred into a Teflon-lined autoclave with a capacity of 50 mL. The autoclave was heated to 100 °C for 24 h. The resulting product, the branched nanorods of β-MnO_2/FeOOH, was collected by filtration and then washed with deionized water and ethanol. Finally, the branched nanorods of β-MnO_2/FeOOH were treated in air at 450 °C for 2 h to produce the branched nanorods of β-MnO_2/α-Fe_2O_3. In order to demonstrate the superior performance of the branched nanorods in LIBs, both β-MnO_2 nanorods and α-Fe_2O_3 nanorods were prepared for the comparison in electrochemical measurements. The preparation of the α-Fe_2O_3 nanorods was achieved by the similar protocol in the absence of the β-MnO_2 nanorods.

Sample Characterization: XRD patterns were achieved on an advanced X-ray diffractometer (Bruker D8 Adv., Germany), based on Ni-filtered Cu Kα radiation. FESEM images and TEM images were obtained from a field-emission scanning electron microscope (JEOL JSM-6700F) and a transmission electron microscope (JEOL JEM 1011) respectively. HRTEM images were recorded with an analytic transmission electron microscope (JEOL JEM-ARM 200F). The N_2 adsorption/desorption isotherms were obtained by a Quadrasorb SI analyzer at a temperature of 77 K. BET and BJH analyses were conducted to determine the surface area, pore volume, and pore size distribution.

Electrochemical Measurements: The working electrode for electrochemical properties was prepared by 60 wt% active material, 20 wt% conductive carbon black and 20 wt% sodium salt of caboxy methyl cellulose (CMC). In the presence of trace water, the above materials were mixed to produce a slurry. Then, the slurry was coated on a copper foil, and dried under vacuum at 80 °C for 12 h. The resulting foil was roll-pressed and cut into a disc. The typical loading density of the active materials was in the range of 1–2 mg cm^{-2}. After that, a coin-type cell of CR 2032 was assembled in an argon-filled glove box with a lithium foil as the counter electrode, a Celgard 2400 membrane as the separator and a mixture of ethylene carbonate (EC), diethyl carbonate (DEC) and dimethyl carbonate (DMC) (1:1:1, volume ratio) as the electrolyte. The coin-type cell was then used for cyclic voltammetry (CV) profiles, galvanostatic discharge-charge cycling, as well as direct current (DC) resistance. CV profiles were obtained in the range of 0.01–3 V at a scanning rate of 0.1 mV s^{-1} from an electrochemical workstation (LK2005A, Tianjin, China). Galvanostatic discharge-charge cycling was performed between 0.01 and 3 V on a lithium battery cycler (LAND CT-2001A, Wuhan, China) at room temperature. AC EIS was carried out on an electrochemical workstation (Materials Mates 510, Italia) in the frequency range from 0.1 MHz to 0.01 Hz. DC resistance was measured at a pulse of 18 s at every 5% increase of DOD (depth of discharge) or SOC (state of charge). Then, the DC resistance (R_{dc}) could be obtained by $R_{dc} = \Delta U/I$, where ΔU is the voltage variation before and after the interruption.

Supporting Information

Supporting Information is available from the Wiley Online Library or from the author.

Acknowledgements

This work was supported by the 973 Project of China (No. 2011CB935901), Natural Science Foundation of China (no. 91022033, 21071055, 51172076, 21203111), New Faculty Start-up funding in Shandong University, New Century Excellent Talents in University (NCET-10-0369), and Independent Innovation Foundations of Shandong University (2012ZD007), Shan-dong Provincial Natural Science Foundation for Distinguished Young Scholar (JQ201205), and Key Laboratory of Fuel Cell Technology of Guangdong Province. We want to thank Prof. Junqing Hu in Donghua University for greatful help in HRTEM images.

Received: December 20, 2012
Revised: March 23, 2013
Published online: April 30, 2013

[1] a) C. M. Park, J. H. Kim, H. Kim, H. J. Sohn, *Chem. Soc. Rev.* **2010**, *39*, 3115–3141; b) P. Poizot, S. Laruelle, S. Grugeon, L. Dupont, J. M. Tarascon, *Nature* **2000**, *407*, 496–499; c) J. S. Chen, L. A. Archer, X. W. Lou, *J. Mater. Chem.* **2011**, *21*, 9912–9924; d) L. Shen, E. Uchaker, X. Zhang, G. Cao, *Adv. Mater.* **2012**, *24*, 6502–6506; e) H. B. Wu, J. S. Chen, H. H. Hng, X. W. Lou, *Nanoscale* **2012**, *4*, 2526–2542.

[2] a) J. S. Chen, C. M. Li, W. W. Zhou, Q. Y. Yan, L. A. Archer, X. W. Lou, *Nanoscale* **2009**, *1*, 280–285; b) Y. L. Wang, J. J. Xu, H. Wu, M. Xu, Z. Peng, G. F. Zheng, *J. Mater. Chem.* **2012**, *22*, 21923–21927;

c) W. Q. Zeng, F. P. Zheng, R. Z. Li, Y. Zhan, Y. Y. Li, J. P. Liu, *Nanoscale* **2012**, *4*, 2760–2765; d) W. W. Zhou, C. W. Cheng, J. P. Liu, Y. Y. Tay, J. Jiang, X. T. Jia, J. X. Zhang, H. Gong, H. H. Hng, T. Yu, H. J. Fan, *Adv. Funct. Mater.* **2011**, *21*, 2439–2445; e) W. W. Zhou, Y. Y. Tay, X. T. Jia, D. Y. Yau Wai, J. Jiang, H. H. Hoon, T. Yu, *Nanoscale* **2012**, *4*, 4459–4463; f) J. X. Zhu, Z. Y. Lu, M. O. Oo, H. H. Hng, J. Ma, H. Zhang, Q. Y. Yan, *J. Mater. Chem.* **2011**, *21*, 12770–12776; g) Y. S. Luo, J. S. Luo, J. Jiang, W. W. Zhou, H. P. Yang, X. Y. Qi, H. Zhang, H. J. Fan, D. Y. W. Yu, C. M. Li, T. Yu, *Energy Environ. Sci.* **2012**, *5*, 6559–6566; h) L. Yu, Z. Y. Wang, L. Zhang, H. B. Wu, X. W. Lou, *J. Mater. Chem. A* **2013**, *1*, 122–127; i) L. M. Qin, Q. Zhu, G. R. Li, F. T. Liu, Q. M. Pan, *J. Mater. Chem.* **2012**, *22*, 7544–7550; j) Z. X. Yang, G. D. Du, Q. Meng, Z. P. Guo, X. B. Yu, Z. X. Chen, T. L. Guo, R. Zeng, *RSC Adv.* **2011**, *1*, 1834–1840; k) X. M. Wu, S. C. Zhang, L. L. Wang, Z. J. Du, H. Fang, Y. H. Ling, Z. H. Huang, *J. Mater. Chem.* **2012**, *22*, 11151–11158; l) G. D. Du, Z. P. Guo, P. Zhang, Y. Li, M. B. Chen, D. Wexler, H. K. Liu, *J. Mater. Chem.* **2010**, *20*, 5689–5694; m) X. Y. Xue, Z. H. Chen, L. L. Xing, S. Yuan, Y. J. Chen, *Chem. Commun.* **2011**, *47*, 5205–5207; n) D. W. Kim, I. S. Hwang, S. J. Kwon, H. Y. Kang, K. S. Park, Y. J. Choi, K. J. Choi, J. G. Park, *Nano Lett.* **2007**, *7*, 3041–3045.

[3] Y. M. Lin, R. K. Nagarale, K. C. Klavetter, A. Heller, C. B. Mullins, *J. Mater. Chem.* **2012**, *22*, 11134–11139.

[4] a) B. Sun, J. Horvat, H. S. Kim, W. S. Kim, J. Ahn, G. X. Wang, *J. Phys. Chem. C* **2010**, *114*, 18753–18761; b) M. V. Reddy, T. Yu, C. H. Sow, Z. X. Shen, C. T. Lim, G. V. Subba Rao, B. V. R. Chowdari, *Adv. Funct. Mater.* **2007**, *17*, 2792–2799; c) Z. Y. Wang, D. Y. Luan, S. Madhavi, Y. Hu, X. W. Lou, *Energy Environ. Sci.* **2012**, *5*, 5252–5256; d) M. S. Wu, P. C. J. Chiang, *Electrochem. Commun.* **2006**, *8*, 383–388; e) A. L. M. Reddy, M. M. Shaijumon, S. R. Gowda, P. M. Ajayan, *Nano Lett.* **2009**, *9*, 1002–1006; f) H. Xia, M. O. Lai, L. Lu, *J. Mater. Chem.* **2010**, *20*, 6896–6902; g) J. M. Kim, Y. S. Huh, Y. K. Han, M. S. Cho, H. J. Kim, *Electrochem. Commun.* **2012**, *14*, 32–35; h) L. H. Li, C. Y. Nan, J. Lu, Q. Peng, Y. D. Li, *Chem. Commun.* **2012**, *48*, 6945–6947.

[5] J. Jiang, Y. Y. Li, J. P. Liu, X. T. Huang, C. Z. Yuan, X. W. Lou, *Adv. Mater.* **2012**, *24*, 5166–5180.

[6] a) J. Yang, J. H. Zeng, S. H. Yu, L. Yang, G. E. Zhou, Y. T. Qian, *Chem. Mater.* **2000**, *12*, 3259–3263; b) J. Yang, C. Xue, S. H. Yu, J. H. Zeng, Y. T. Qian, *Angew. Chem. Int. Ed.* **2002**, *41*, 4697–4700; c) J. Yang, T. W. Liu, C. W. Hsu, L. C. Chen, K. H. Chen, C. C. Chen, *Nanotechnology* **2006**, *17*, S321–S326.

[7] M. S. Wu, P. C. J. Chiang, J. T. Lee, J. C. Lin, *J. Phys. Chem. B* **2005**, *109*, 23279–23284.

[8] X. L. Wu, Y. G. Guo, L. J. Wan, C. W. Hu, *J. Phys. Chem. C* **2008**, *112*, 16824–16829.

[9] a) J. Z. Zhao, Z. L. Tao, J. Liang, J. Chen, *Cryst. Growth Des.* **2008**, *8*, 2799–2805; b) W. Xiao, J. S. Chen, Q. Lu, X. W. Lou, *J. Phys. Chem. C* **2010**, *114*, 12048–12051; c) B. Wang, J. S. Chen, H. B. Wu, Z. Y. Wang, X. W. Lou, *J. Am. Chem. Soc.* **2011**, *133*, 17146–17148.

[10] R. Dedryvère, S. Laruelle, S. Grugeon, P. Poizot, D. Gonbeau, J. M. Tarascon, *Chem. Mater.* **2004**, *16*, 1056–1061.

[11] H. Lai, J. X. Li, Z. G. Chen, Z. G. Huang, *ACS Appl. Mater. Interfaces* **2012**, *4*, 2325–2328.

[12] C. X. Guo, M. Wang, T. Chen, X. W. Lou, C. M. Li, *Adv. Energy Mater.* **2011**, *1*, 736–741.

[13] Y. F. Deng, Q. Zhang, S. Tang, L. Zhang, S. Deng, Z. Shi, G. H. Chen, *Chem. Commun.* **2011**, *47*, 6828–6830.

[14] P. Balaya, H. Li, L. Kienle, J. Maier, *Adv. Funct. Mater.* **2003**, *13*, 621–625.

[15] a) C. Li, W. Wei, S. M. Fang, H. X. Wang, Y. Zhang, Y. H. Gui, R. F. Chen, *J. Power Sources* **2010**, *195*, 2939–2944; b) P. C. Lian, S. Z. Liang, X. F. Zhu, W. S. Yang, H. H. Wang, *Electrochim. Acta* **2011**, *58*, 81–88.

[16] H. Y. Xu, S. Xie, N. Ding, B. L. Liu, Y. Shang, C. H. Chen, *Electrochim. Acta* **2006**, *51*, 4352–4357.

[17] Z. C. Bai, B. Sun, N. Fan, Z. C. Ju, M. H. Li, L. Q. Xu, Y. T. Qian, *Chem. Eur. J.* **2012**, *18*, 5319–5324.